Available online at www.sciencedirect.com

ScienceDirect

Advances in Space Research xxx (2019) xxx–xxx

ADVANCES IN SPACE RESEARCH (a COSPAR publication)

www.elsevier.com/locate/asr

Constrained scales in ocean forecasting

Gregg A. Jacobs [a,*], Joseph M. D'Addezio [a], Brent Bartels [b], Peter L. Spence [b]

[a] 1009 Balch Blvd, Naval Research Laboratory, Stennis Space Center, MS 39529, USA
[b] 1009 Balch Blvd, Perspecta, Stennis Space Center, MS 39529, USA

Received 28 February 2019; received in revised form 5 September 2019; accepted 7 September 2019

Abstract

Observation space-time resolution limits the scales at which ocean forecast systems provide skillful information. The ocean processes of concern are mesoscale instabilities for which an ocean forecast system requires regular corrections of initial conditions to maintain skillful forecasts, and the observations considered are the regular satellite and in situ. Predominantly, the satellite altimeter constellation is the main observing system for this problem. We define constrained scales as those in which the forecast system has skill. The constrained scales are determined by successively filtering small-scale variability from 1 km resolution assimilative model experiments to reach a minimum error relative to ground truth data. Independent observations are from the LAgrangian Submesoscale ExpeRiment (LASER) consisting of over 1000 surface drifters persisting for three months in the Gulf of Mexico. We also vary the decorrelation scale of the assimilation system to determine the decorrelation scale that produces the smallest forecast trajectory errors. In present ocean forecast systems using regular observations, the constrained scales are larger than defined by a Gaussian filter with e-folding scale of 58 km or ¼ power point of 220 km. The decorrelation scale of 36 km used in the assimilation second order auto-regressive correlation function provides lowest trajectory errors. Filtering unconstrained variability from the model solutions reduces trajectory errors by 20%. Published by Elsevier Ltd on behalf of COSPAR.

Keywords: Altimeter; Ocean model; Assimilation; Drifters; Prediction

1. Introduction

Satellite altimeter observations have become a critical data stream to enable ocean forecasts (Le Traon et al., 2017). Ocean mesoscale eddies have horizontal length scales on the order of 200 km in tropical latitudes to 20 km at high latitudes, and these features are instability processes (Chelton et al., 1998; Jacobs et al., 2001). Ocean models integrate initial conditions forward in time, and any error in the initial state grows exponentially. At some point in the forecast period, the ocean model features have realistic energy, amplitude, and size, but positions are not coincident with those in the real world (Thoppil et al., 2011). Satellite altimeters are the primary source of observations that regularly correct the initial conditions of model forecasts. In this examination, we are concerned with the regular ocean observations that are typically available rather than targeted observations that are limited in space and time for particular features.

There are many ocean forecast applications requiring continual predictions of ocean temperature and salinity structure as well as transports of material (Bell et al., 2015). These include fisheries management, search and rescue operations, aquaculture farming, and many others. The Macando oil platform incident is one such example in which accurate surface oil transport forecasts were needed to prepare cleanup efforts and understand the transport of oil (Özgökmen et al., 2016). If accurate forecasts are required for the public good, we must quantify the features

* Corresponding author.
E-mail addresses: gregg.jacobs@nrlssc.navy.mil (G.A. Jacobs), joseph.daddezio@nrlssc.navy.mil (J.M. D'Addezio), brent.bartels.ctr@nrlssc.navy.mil (B. Bartels), Peter.Spence.ctr@nrlssc.navy.mil (P.L. Spence).

https://doi.org/10.1016/j.asr.2019.09.018
0273-1177/Published by Elsevier Ltd on behalf of COSPAR.

skillfully predicted by ocean models that rely on regular observing networks.

Any observing system has limits in the resolved time and space scales, and these lead to limitations in the scales of ocean model features that are predictable. We can run ocean models at high resolutions to represent the physics of small features, but satellite observing systems may not provide the necessary observations to resolve those features. We use the term *constrained* to refer to the features in an ocean model prediction for which there are sufficient observations to produce a skillful forecast on average, and *unconstrained* for features that do not have sufficient observations for a skillful forecast on average. As an example, consider Fig. 1 that shows the surface currents of a numerical ocean model continually corrected by satellite observations compared to a set of GPS-tracked surface drifters. These drifters were deployed as part of the LAgrangian Submesoscale ExpeRiment (LASER) campaign conducted by the Consortium for Advanced Research on Transport of Hydrocarbon in the Environment (CARTHE) (Özgökmen et al., 2018). Many drifters returned position information for over three months. The ocean model did not use the drifter information in the daily assimilation and forecast. The large-scale model features are generally aligned with observed drifter trajectories, though small-scale features in the model do not align with the drifter observations. A smaller scale example is shown by the model field at two times, seven days apart (Fig. 2). At the initial time, the model cyclone and cyclone in the drifter observations are not well aligned. At the final time, the model cyclone is aligned more correctly with the drifters. The right two panels in Fig. 2 show all the satellite altimeter data that observed this feature during the seven days. As we will demonstrate through our experimentation, features of this size are at the limits of being constrained because the satellite observations are not sufficient to ensure regular corrections of the model to maintain accurate positioning at all times.

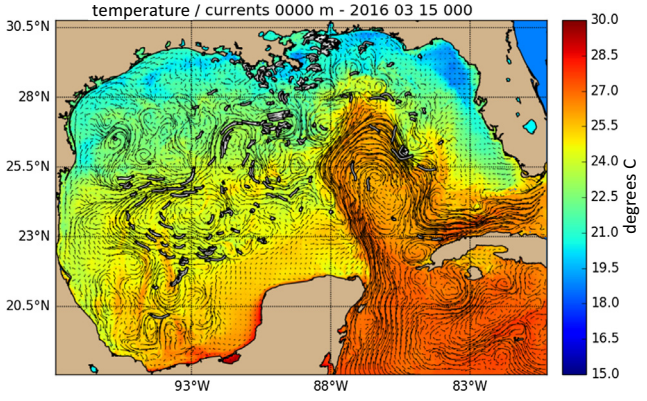

Fig. 1. An example on March 15, 2016 00 GMT of the ocean model surface currents (black vectors indicate 24 h trajectories given time-fixed model currents), surface temperature (color), and LASER drifter trajectories over 24 h (white lines). Larger scale features show general agreement, while smaller scale features are not well aligned between the model and observations.

We can more rigorously define the separation of constrained and unconstrained scales through the power spectral density (PSD) of the ocean fields. Constrained wavelengths are those in which the PSD of the errors (model-estimated field minus the true field) is less than the PSD of the true field. That is, at a given wavelength, if the model forecast has skill then the variance of the errors is less than the variance of the true field. D'Addezio et al. (2019) used this definition to estimate the constrained scales to be approximately 160 km when considering the sea surface height (SSH). The study used an Observing System Simulation Experiment (OSSE). First, the Nature Run is a realistic numerical model with no observations correcting it. Observing systems sample the Nature Run as the observing systems sample the true world, and the simulated observations correct a second model. The full time-evolving 3D fields of the Nature Run and OSSE model provide the error PSD and thus the constrained scales.

However, there are cautions in OSSEs that may lead to incorrect conclusions (Atlas et al., 2015). For example, the study by D'Addezio et al. (2019) used fraternal twin models in which the Nature Run and the assimilative runs used the same dynamical system at the same resolution. The study intended to examine the effect of observations under the assumptions that the dynamical representation and assimilation systems are accurate and not significant contributors to analysis and forecast errors. In the examination at hand, we add to this prior study by retaining the effects of the dynamical system and data assimilation errors, and we use the dense drifter observations from LASER to estimate the constrained scales. Our basic question is then, what are the constrained scales enabled by the regular observations of the true world in present forecast systems?

In the future we expect the satellite observing network to expand with the deployment of the Surface Water/Ocean Topography (SWOT) mission in 2021 (Gaultier et al., 2016). Present altimeter satellites measure SSH only at the satellite nadir point. SWOT will provide observations across a 120 km swath at 1 km resolution. While the data will be high-resolution spatially, a planned 21-day repeat cycle will result in dense but patchy data on a daily basis. The traditional nadir altimeters are low-resolution between SWOT ground tracks and provide the larger scale observations. Therefore, the SWOT observations will be a dense patch of data within a larger set of coarser observations. Additionally, expendable bathythermographs, ocean underwater gliders, profiling floats, and dense drifter deployments often provide targeted observations. Similar to the SWOT situation, targeted in situ sampling can provide dense patchy data within the context of the coarser regular observations.

An approach for correcting a model initial condition for this situation is through a multiscale analysis technique (Li et al., 2015) in which scales resolved by the coarse

Please cite this article as: G. A. Jacobs, J. M. D'Addezio, B. Bartels et al., Constrained scales in ocean forecasting, Advances in Space Research, https://doi.org/10.1016/j.asr.2019.09.018

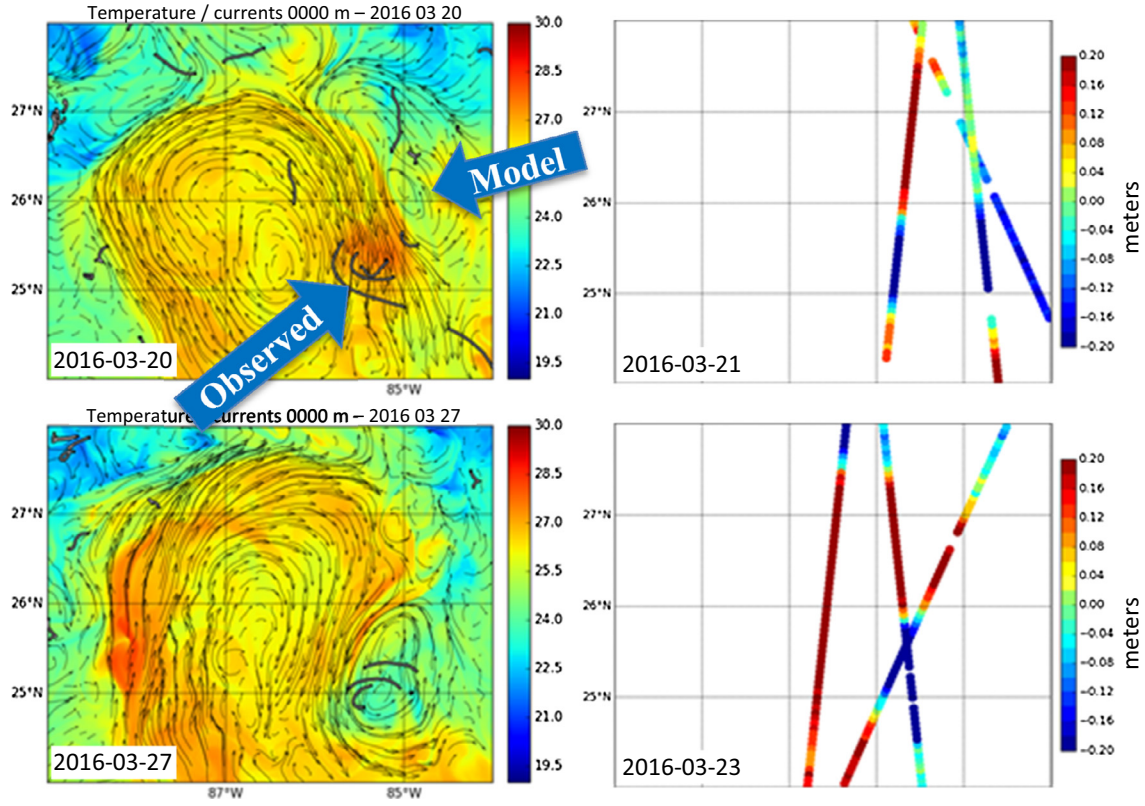

Fig. 2. On March 20, 2016, the model cyclone feature is not well aligned with the LASER drifter tracks (top left), while the model feature is better aligned (bottom left) after the altimeter observations during a seven day period (right column) are assimilated into the model. The model plots (left) show surface currents (black vectors indicate 24 h trajectories given time-fixed model currents), surface temperature in degrees C (color), and LASER drifter trajectories over 24 h (thick black lines). The altimeter observations show sea surface height anomaly (SSHA) in meters that were observed during the indicated days.

observations are first corrected, and then smaller scales resolved by patchy dense data are corrected. In this two-step methodology, a critical parameter is the analysis scales that separate the first and second assimilation steps. Quantifying the presently constrained scales in the forecast model can provide an estimate of this parameter.

Within the correction of the model initial condition, an observation influences a surrounding area through a specified scale. Formally, this represents the spatial correlation of errors in the model initial condition. The size of this decorrelation scale could influence the constrained scales. Thus, at the same time we are estimating the constrained scales, we examine the effects of the decorrelation scale and determine if this changes the constrained scales.

To address these issues, our analysis involves running five different ocean model experiments. Each experiment assimilates all regular observations (and not the LASER drifter data) using a different decorrelation length scale. Prior work addressing the issue of constrained and unconstrained model features determined constrained scales using wavenumber spectral analysis (D'Addezio et al., 2019). However, this approach cannot be used here because the drifter observations do not provide full 2-dimensional fields, and the drifter observations are not sufficiently dense to estimate the wavenumber spectra down to sufficiently small scales. Instead, the approach we use is to spatially filter the surface velocity field from each model experiment using a range of filter scales. The filtering scale at which the errors are minimum relative to the LASER observations provides the scale at which forecast errors equal the ocean variability. The optimal decorrelation scale is shown to be about 36 km (the length scale of a second order autoregressive function), and the associated constrained scales are 220 km (the ¼ power wavelength of a Gaussian filter). For the experiment with the lowest errors, the trajectory error reduction from no filtering to the lowest error point is about 20%.

We describe in Section 2 the numerical ocean model along with the assimilation method that corrects the model with the observations. Section 3 describes the LASER data and initial comparisons to the model results. Section 4 provides the details of the methodology to filter small scales from the model experiments and provides the overall results. Finally, the results are summarized and conclusions provided.

2. Model and assimilation setups

The experiments use the ocean prediction system in operational application (Rowley and Mask, 2014) com-

Please cite this article as: G. A. Jacobs, J. M. D'Addezio, B. Bartels et al., Constrained scales in ocean forecasting, Advances in Space Research, https://doi.org/10.1016/j.asr.2019.09.018

posed of the Navy Coastal Ocean Model (NCOM) (Martin et al., 2009) with the 3DVar Navy Coupled Ocean Data Assimilation (NCODA) (Smith et al., 2011). The Fleet Numerical Meteorology and Oceanography Center (FNMOC) uses this system operationally for predicting high-resolution areas (down to 200 m resolution) nested in the global ocean prediction system. The domain for our experiments is the entire Gulf of Mexico modeled at 1 km horizontal resolution with 50 vertical levels. The setup uses 34 terrain-following sigma coordinates above 550 m depth and 16 Z level coordinates below 550 m. The vertical coordinate structure has higher resolution near the surface with the surface layer having 0.5 m thickness. Boundary conditions are from the global HYbrid Coordinate Ocean Model (HYCOM) (Metzger et al., 2010). Boundary conditions for barotropic tidal currents and elevation were applied from the Optimal Tide Interpolation System (OTIS) (Egbert and Erofeeva, 2002). The model forcing also includes tidal potential. Atmospheric forcing from the Coupled Ocean Atmosphere Mesoscale Prediction System (COAMPS) (Hodur, 1997) along with the ocean model surface temperatures provide estimates of surface momentum flux, latent and sensible heat flux, and solar radiation penetration into the water column.

The system runs a daily cycle of assimilation and forecast in which all observations go to NCODA, which then provides a correction to the initial condition for NCOM. The NCOM forecast becomes the background for the next NCODA update cycle. Operationally, altimeter sea surface height anomaly (SSHA) during this period from Jason-2, CryoSat-2, and AltiKa arrive with 24- to 48-hour latency, which is the difference between observation time and the assimilation time. The experiments here are hindcast experiments, so data latency is not an issue. Each experiment begins with the same initial condition on October 1, 2015 provided by the same 1 km cycling assimilation system that began running in 2012 (Jacobs et al., 2016). After initialization, each experiment ran independently using all the regular observations. Beginning the experiments more than 100 days prior to the LASER observations allows each system to execute many assimilation cycles. The long assimilation spin-up removes influence of the initial condition on October 1, 2015 from affecting evaluations relative to drifter trajectories starting January 16, 2016.

The satellite altimeter SSHA is the dominant information source for updating and constraining the mesoscale field. Within the NCODA assimilation, SSHA observations along with the Modular Ocean Data Assimilation System (MODAS) vertical covariance information (Fox et al., 2002) provide a synthetic temperature and salinity profile, and the synthetic profile is used in the 3DVar assimilation. Observations minus the background are the innovations d. The 3DVar analysis produces the increment δx defined by:

$$\delta x = BH^T\left(HBH^T + R\right)^{-1} d \tag{1}$$

where R is the covariance of observation errors (assumed to be diagonal), H is the observation operator that maps from the model state to the observation values, and B is the background error covariance represented by a diagonal standard deviation matrix S and a correlation matrix so that $B = SCS$. A decomposition of the correlation matrix C into separable functions is made so that the correlation between two model variables v and v' is given by

$$C_{vv'}(x,y,z,t,x',y',z',t') = C^H_{vv'}(x,y,x',y')C^V_{vv'}(z,z')C^{FDB}_{vv'}(x,y,x',y') \tag{2}$$

where the two variables are noted by v and v' at the locations (x,y,z) and (x',y',z') respectively. The vertical correlation $C^V_{vv'}(z,z')$ is a function of the vertical density gradient so that portions of the water column with high vertical gradients have shorter decorrelation scales. The horizontal correlation function is a second order autoregressive (SOAR) function:

$$C^H_{vv'}(x,y,x',y') = (1 + s/L_c)e^{(-s/L_c)} \tag{3}$$

where s is the horizontal distance between the two points $|(x-x',y-y')|$, and L_c is the prescribed decorrelation length scale. The decorrelation scale is related to the Rossby radius of deformation multiplied by a scaling factor *rscl*. Fig. 3 provides an example of the horizontal SOAR with a decorrelation scale of 1.0 for reference. In comparison to a Gaussian function with an e-folding scale of 1.0, the SOAR function has larger amplitudes. The point at which the filter amplitude normalized by the wavenumber 0 amplitude has a value of ½, or the squared amplitude has a value of ¼, is a characterization of a filter. For the SOAR, the ¼ power wavelength is about 11 times the decorrelation scale.

The flow-dependent correlations are $C^{FDB}_{vv'}(x,y,x',y') = (1 + s_f)e^{-s_f}$, where $s_f = |SSH(x,y) - SSH(x',y')|/dh$, and dh is the specified flow-dependent scale factor. The value of dh was 0.12 m in the experiments. This decreases correlation between areas where SSH differs and maintains the correlation between areas of similar SSH. The SSH field is used in the flow-dependent correlation under the assumption that the flow is directed along pressure surfaces (i.e. the flow is in geostrophic balance) due to mesoscale features.

We vary the value of *rscl* across the experiments to control the influence distance of observations. The Rossby radius of deformation varies spatially, and the spatially averaged decorrelation values for the five experiments are shown in Table 1. All other inputs and settings are the same across the experiments. All experiments use the same regular observing systems. The regular data consisted of the altimeter satellites Jason-2, CryoSat-2, and AltiKa as well as satellite sea surface temperature and available in situ profiles. The in situ observations are very sparse. The increments resulting from Eq. (1) on one day (Fig. 4) indicate the spatial influence scale impact across the experiments. Experiment A has the shortest decorrelation scale, and the increments from the altimeter data are localized

Please cite this article as: G. A. Jacobs, J. M. D'Addezio, B. Bartels et al., Constrained scales in ocean forecasting, Advances in Space Research, https://doi.org/10.1016/j.asr.2019.09.018

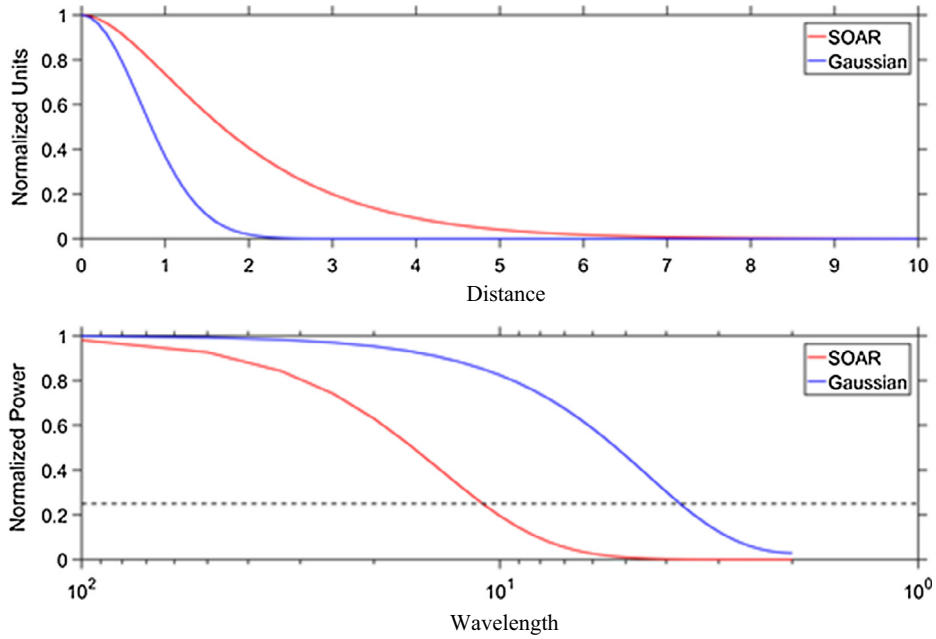

Fig. 3. The SOAR decorrelation function and a Gaussian function each with a length scale of 1 (top), and the squared amplitude of the Fourier transforms normalized by the value at 0 wavenumber (bottom). The ¼ power level is marked in the lower plot by the dashed line.

Table 1
The five experiments, the *rscl* values, and the spatial mean decorrelation lengths L_c are provided. All other parameters are the same across experiments.

Experiment	*rscl*	Mean L_c (km)
A	0.4	9
B	1.2	23
C	2.0	36
D	4.4	78
E	6.5	114

along the satellite tracks. The spatial decorrelation scale increases through experiment B and C, and the innovations influence points further from the ground tracks. As scales further increase in experiments D and E, the flow dependent influence is apparent near the Loop Current. The correlation between two locations is a product of the horizontal and flow-dependent correlation according to (2). When the horizontal length scale is very small, the SSH does not vary significantly within the distance of the flow-dependent scale. Therefore, the effects of the flow-dependent correlation are not apparent in experiments A-C. As the horizontal length scale increases, the SSH changes significantly within the range of the flow-dependent scale, and the flow-dependent effects become more apparent in experiments D and E. Examination of several other aspects of the assimilation are provided in Jacobs et al. (2014) in which the flow-dependent correlation did not have significant effect on the forecast skill.

Note that because the experiments are independent, each has slightly differently placed features and different error levels. While the observations for each experiment are the same, the prior forecast, used as the background, is different, and the innovations computed from the background and observations for each experiment are different. Therefore, there is more than just the length scale producing differences in the increments of the experiments of Fig. 4.

The spatial scales within the increments motivate a question: Does the data assimilation affect the small-scale energy of the ocean prediction? The system divides the 3DVar analysis increment by the number of time steps in the insertion interval (6 h for these experiments), and every model time step adds a fraction of the increment to the state. The process does not force the model state to match the increment field plus the background as nonlinear evolution occurs during the insertion interval. The process allows small-scale features in the ocean model to develop. A qualitative examination of the surface currents and temperature (Fig. 5) indicates all the experiments contain small-scale features down to approximately 10 km.

To quantify the energy across scales, we compute the PSD of the surface kinetic energy from the model. A sub domain is chosen that contains no land values (22°–28°N, 86°–93°W), and the 2D FFT of the velocity field components is taken over the domain at 6 h intervals between January 1 and May 1, 2016. The 2D FFT is averaged in time and then averaged azimuthally to provide the one-dimensional spectrum for each velocity component. The PSD of the kinetic energy is given by PSD(KE) = [PSD(u) + PSD(v)]/2 (Richman et al., 2012). The Nyquist wavelength is 2 km due to the 1 km model grid, which limits the PSD range (Fig. 6 top). A least squares fit to the PSD between 10 km and 200 km wavelengths of all experiments results in a mean slope of −3.4. The PSD energy of all experiments does not deviate substantially from the

Please cite this article as: G. A. Jacobs, J. M. D'Addezio, B. Bartels et al., Constrained scales in ocean forecasting, Advances in Space Research, https://doi.org/10.1016/j.asr.2019.09.018

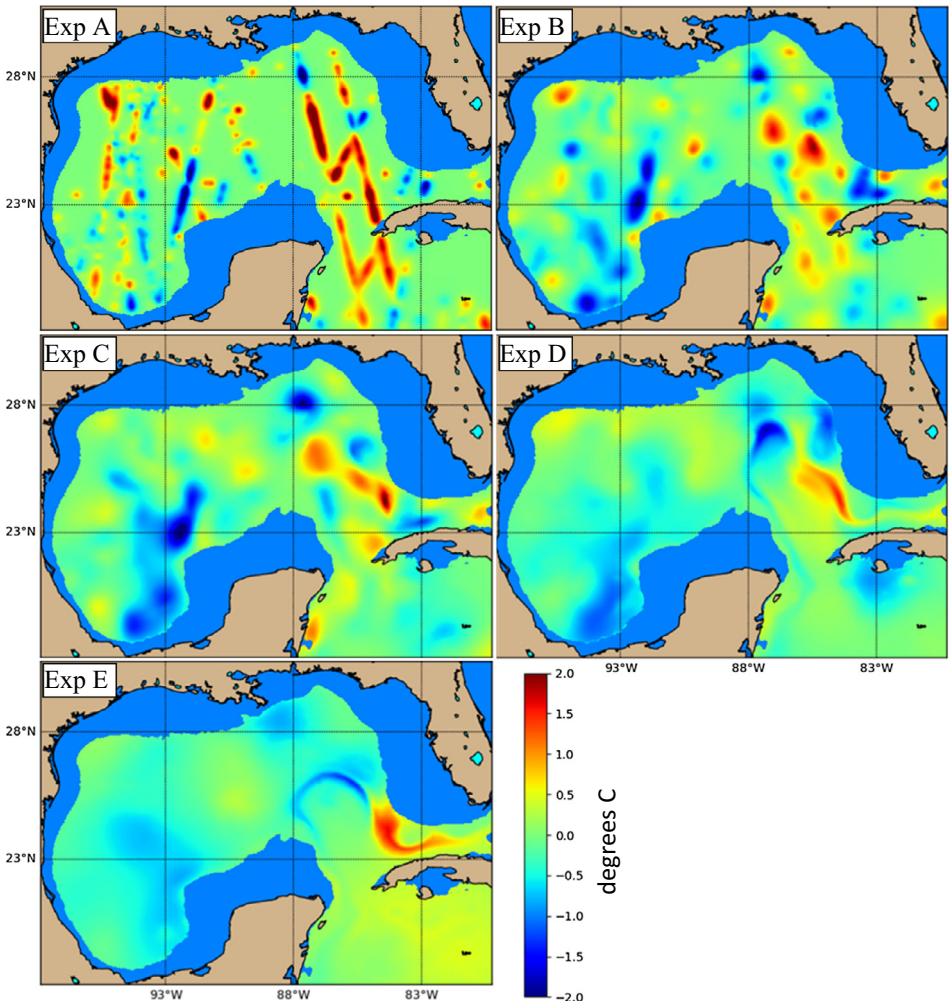

Fig. 4. The 3DVar increment to temperature at 200 m on March 15, 2016 provides an example of the decorrelation scale effects across the five experiments. The satellite tracks are apparent in experiment A with very localized increments. The flow dependent correlation influence is apparent in experiments D and E around the edge of the Loop Current.

−3.4 slope until scales smaller than about 10 km, which is the smallest scale feature a 1 km numerical model should resolve. Thus, we have some confidence that the model numerics are representing the cascade of energy from larger scales into those scales represented by the 1 km grid.

The assimilation process is adding a field to the numerical model every assimilation cycle. This acts as a forcing to the physics represented by the model. The spatial scale of the forcing is the horizontal decorrelation scale of each experiment, and Fig. 3 shows the Fourier transform of the SOAR function with a scale of 1.0. The numerical model physics will transfer the forcing energy to other scales as small eddies coalesce into larger eddies and energy moves to smaller scales through dissipation. Differences in the energy spectra between the experiments can provide some insight as to the effects of the assimilation process, so small deviations from the mean −3.4 slope line are important, and the ratio of each experiment PSD to this line is examined (Fig. 6 bottom). In the mid-scale band of 50 to 200 km wavelengths, experiment A contains higher energy, and experiment B also contains above average energy. In the small-scale band of 10–30 km, experiments E and D contain higher energy.

The differences in each experiment PSD are indicative of the data assimilation effects, though some caution is necessary. The spectra are obtained by averaging over space and time, and the 3 month period is relatively long to small features (less than 100 km wavelength) though is not long relative to large features such as the Loop Current Eddy. The spatial area may also bias the results. In addition, to fully evaluate the assimilation impact on the PSD, a free running model result is required, which was not conducted in this study.

The PSD, however, do indicate some possible sources for the results. The decorrelation scale for experiment A is 9 km (Table 1), and therefore the ¼ power wavelength of the SOAR (Fig. 3) is about 99 km. One interpretation of Fig. 6 is that the assimilation cycle in experiment A is forcing energy at these scales. Experiment B has slightly elevated energy in the 50–100 km band as well. Experi-

Please cite this article as: G. A. Jacobs, J. M. D'Addezio, B. Bartels et al., Constrained scales in ocean forecasting, Advances in Space Research, https://doi.org/10.1016/j.asr.2019.09.018

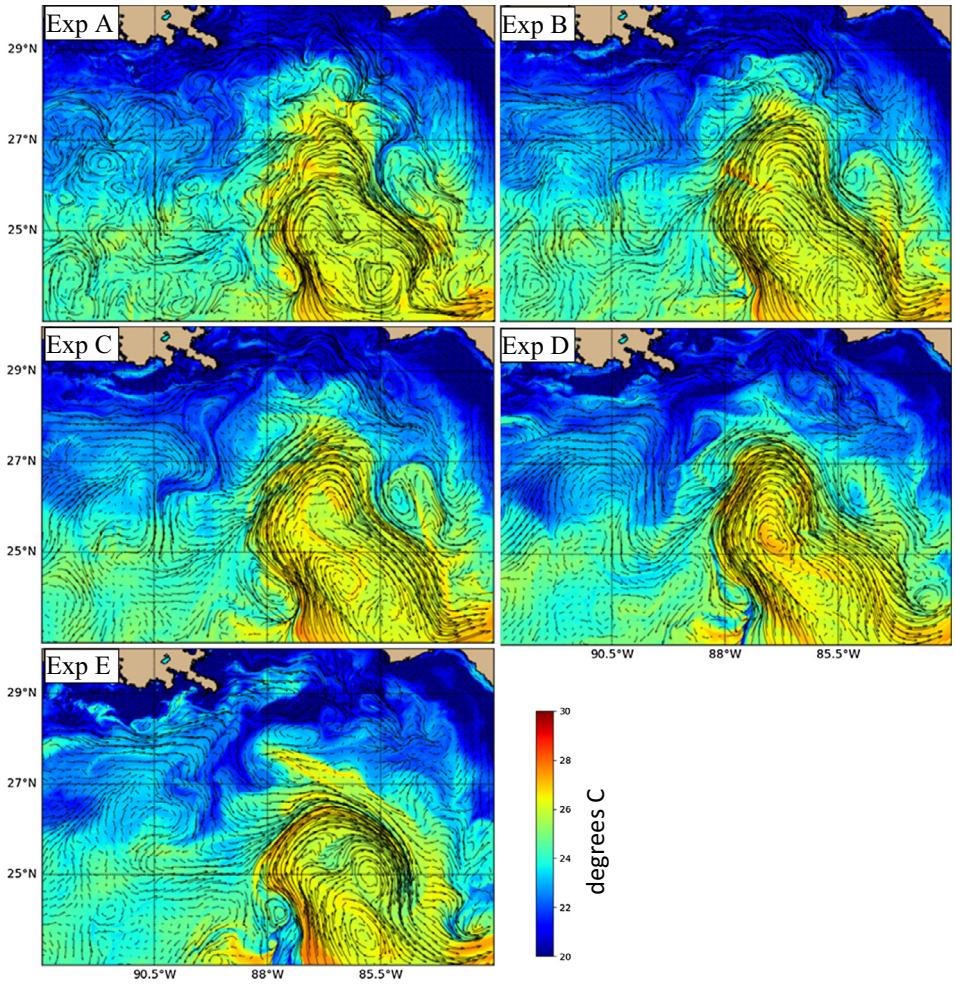

Fig. 5. An example of the surface currents (black vectors indicate 24 h trajectories given time-fixed model currents) over surface temperature (color) on March 15, 2016 from the five experiments indicates all experiments contain small-scale features. Experiment A appears to contain stronger variability at 100 km scales. (For interpretation of the references to color in this figure legend, the reader is referred to the web version of this article.)

ments C-E do not indicate the additional energy in this band. The energy in the 10–50 km range increases successively from C through E. The features appearing in this small-scale band are difficult to observe in the velocity field because the PSD levels at the 100 km wavelength are $10^{3.4}$ times larger than at the 10 km wavelength. The features are more discernable if we examine gradients of the velocity field. The Okubo-Weiss parameter is the shear strain squared plus normal strain squared minus vorticity squared. This removes shear along fronts and the vortices are more clear (Fig. 7). Experiments D and E in Fig. 7 contain more of the 10–20 km vortices compared to experiments A and B.

Experiment E contains about 35% more energy than experiment C at 20 km wavelengths. The largest decorrelation scale of experiment E is potentially leaving the scales around 20 km the least disturbed. Therefore, it appears that the very short decorrelation scales of experiment A are adding noise to the system that disrupts the small scales, and longer decorrelation scales do not disturb the small-scale features. The physical process resulting in the higher energy at 10–50 km in experiments D and E is not definitively demonstrated here, and the subject remains an open question for future consideration.

3. LASER observations

The LASER drifter system consisted of over 1000 surface drifters (Özgökmen et al., 2018). The drifter form was a toroidal float with a GPS receiver and a drogue attached to the center. The drifters were tested in laboratory facilities, and the portion of the water column observed is the upper 0.6 m (Novelli et al., 2017). Ships deployed the drifters starting on January 16, 2016. Initial deployments in the northeastern Gulf of Mexico were in pre-planned patterns constructed in fractal arrangements to understand the relative dispersion across scales of 100 m to 100 km. Further ship deployments occurred in subsequent weeks within submesoscale features identified by aircraft-observed sea surface temperature. Extreme convergence showed rapid clustering of drifters into small areas (D'Asaro et al., 2018). Deployments around the fresh

Please cite this article as: G. A. Jacobs, J. M. D'Addezio, B. Bartels et al., Constrained scales in ocean forecasting, Advances in Space Research, https://doi.org/10.1016/j.asr.2019.09.018

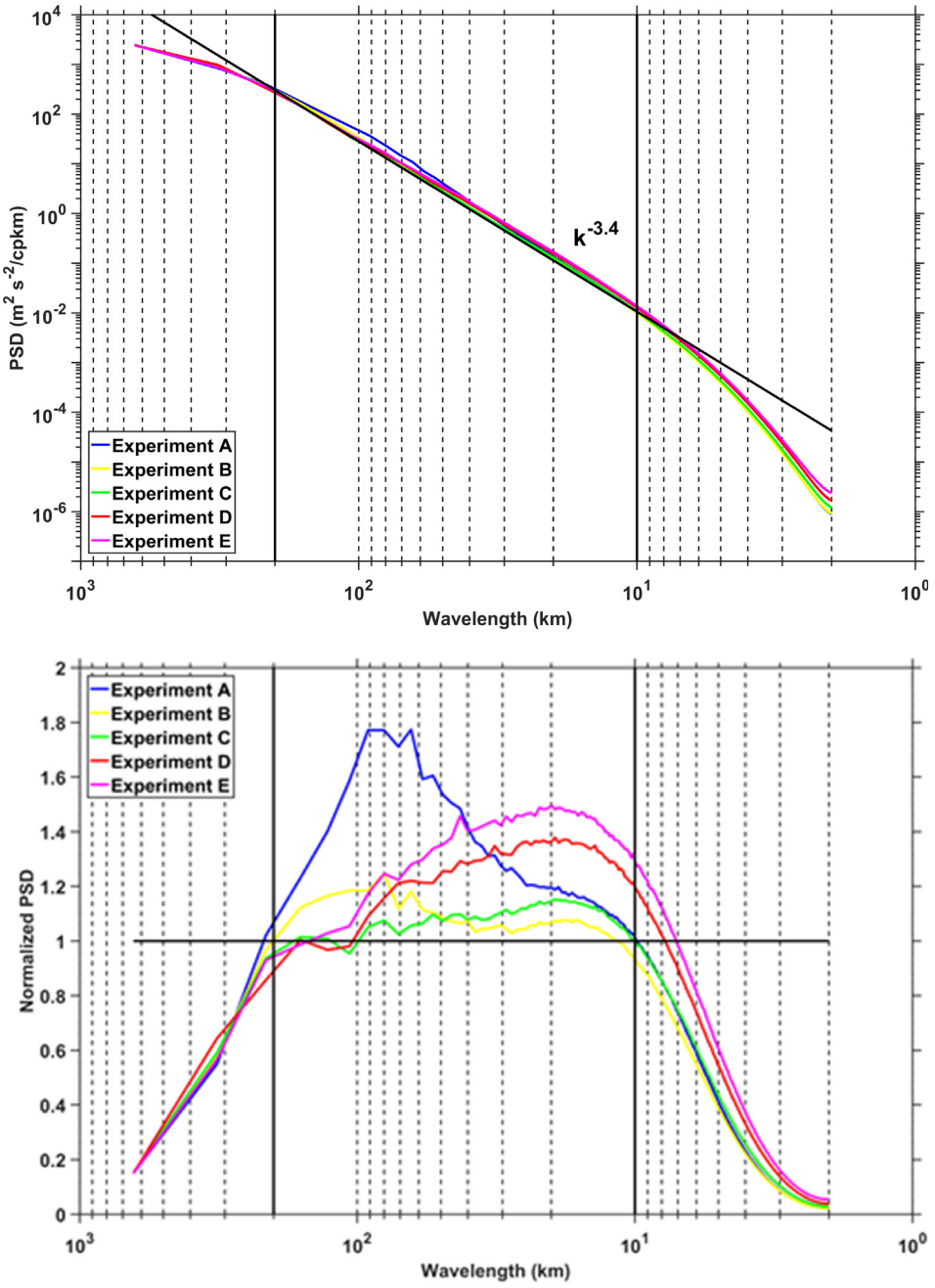

Fig. 6. The wavenumber power spectral density (PSD) of surface kinetic energy from the five experiments (top) have an average slope of −3.4 from 10 to 200 km. The ratio of PSD of each experiment to the −3.4 line (bottom) shows the effects of the small decorrelation scale in experiments A and B injecting energy at the 50–100 km range.

water fronts of the Mississippi River outflow increased the drifter density in the northeastern Gulf of Mexico. By February 10, 2016, there were over 1000 drifters in the observing system. The typical battery life of the drifters was 90 days, though many events occurred to decrease the useful drifter life. The drogue on some drifters detached leaving the drifter more subject to wind effects and therefore less accurate in measuring surface ocean currents. An extensive effort succeeded in identifying the times at which drifters lost drogues, and these were shown to be related to large wind and subsequent wave events (Haza et al., 2018). The analysis here uses only the drifter data from the periods identified as having a drogue. The drifters reported GPS position every 5 min, and additional efforts filtered erroneous GPS positions and noise from the returned data. In addition to restricting consideration to only drifters with a drogue, we also restrict data to be in water depths greater than 500 m. The dynamics over the continental shelf are very constrained by bathymetric geometry. We are concerned with the instabilities generated

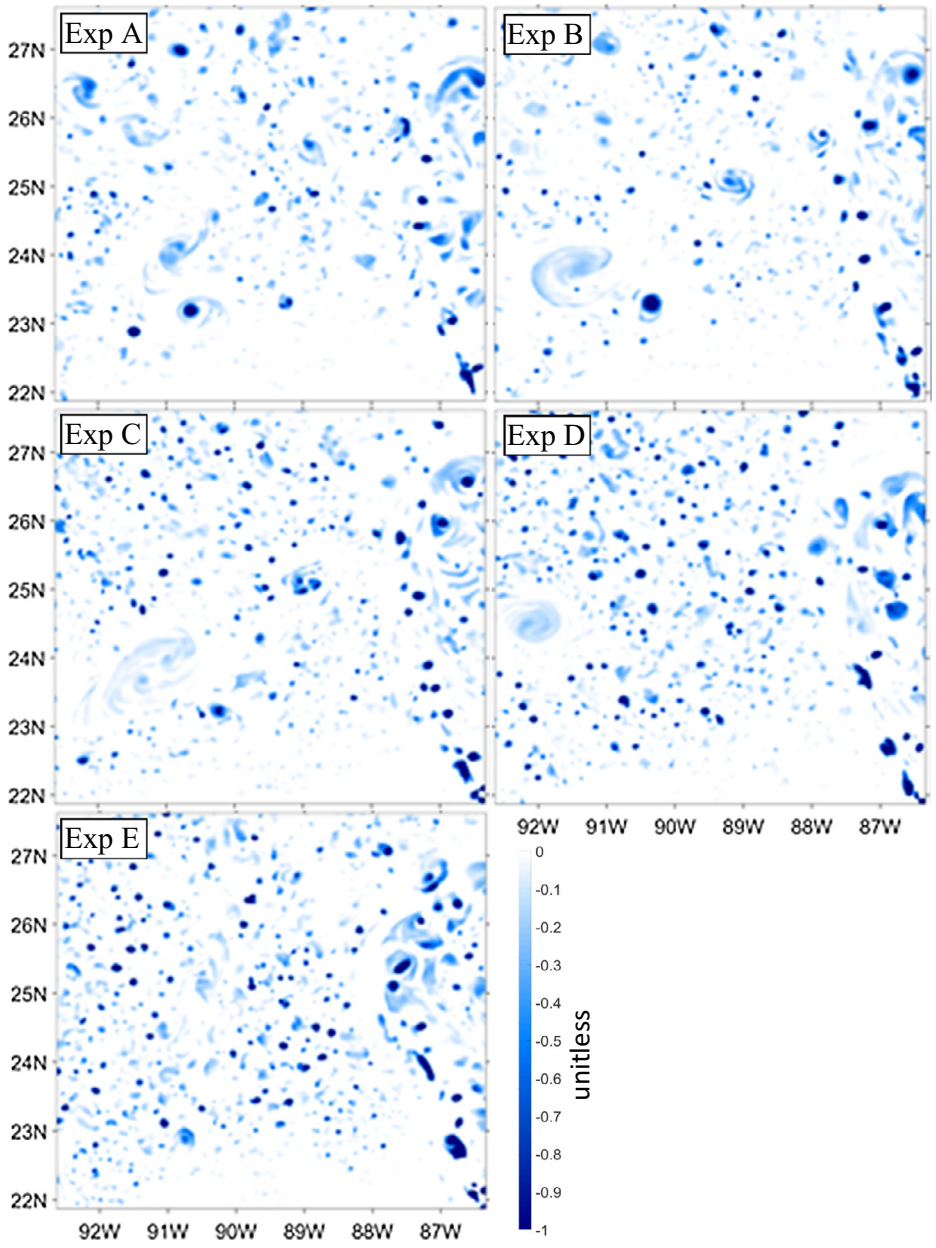

Fig. 7. Okubo-Weiss parameter normalized by the spatial standard deviation computed from surface currents of the five experiments indicates the larger number of 10–20 km features in experiments D and E.

within the ocean interior and reflected by the mesoscale field. Regular correction of these instabilities is the objective of the data assimilation.

In comparing the LASER observations to the model results, we integrate model-simulated trajectories over time. The trajectory integration started at 00 GMT on every day of the LASER experiment. At 00 GMT, we initialize particles in the model surface velocity field at the observed locations. We integrate particle trajectories forward in time through the model velocity field. At the local time of one inertial period, we difference the observed drifter and model particle position to determine the error, and we convert this to an average speed error in km/day.

We use this approach for two reasons. One is to reduce the influence of GPS noise by using positions separated by a long time. The error due to GPS noise decreases as the time interval between position differences increases. The second reason is to reduce errors in wind forcing on the model forecasts. Typically, an impulsive wind forcing will generate an inertial oscillation in the ocean that is a balance between the Coriolis force and horizontal velocity acceleration. These inertial oscillations result in trajectories that form circles over an inertial period, which are superimposed on the other flow features. Errors in wind forcing can result in large errors between the instantaneous model and observed velocities. Because we are comparing position

Please cite this article as: G. A. Jacobs, J. M. D'Addezio, B. Bartels et al., Constrained scales in ocean forecasting, Advances in Space Research, https://doi.org/10.1016/j.asr.2019.09.018

at the end of the inertial period, we reduce errors due to wind forcing on the model. The inertial period ranges from 1.45 days at 20°N to 1.00 days at 30°N. Computations use the local inertial period for each drifter when evaluating trajectory errors.

Because of the relatively long drifter life, the drifters covered a very wide area within the Gulf of Mexico (Fig. 1). This is important for having many samples over many different events to increase the number of independent error estimates. Drifters within a group covering a small spatial area of a large feature are not providing independent estimates of error. Therefore, we process many observations in one small area to produce a single super-error, ultimately preventing situations where many error estimates provide redundant data resulting in the over-weighting of an error. To construct super-errors, for the analysis conducted on each day, the root mean square (RMS) of all error values within each cell of a 1/8° grid over the Gulf of Mexico contribute to one super-error estimate. Thus, the maximum number of super-errors in any cell is the number of days in the deployment. The spatial distribution of the number of super-errors (Fig. 8) indicates coverage throughout much of the domain. Because a relatively long time is required for drifters to move from the original deployment location in the northeastern Gulf of Mexico, there is a substantial concentration of data in the deployment area. Still, the observation density covers a broad region, sampling many different features and events.

An evaluation of the model errors can be visualized in the form of a vector error histogram (Fig. 9). The bin in which a vector difference is included uses the direction difference between observation and model to determine the angle (an angular difference of 0 is along the line from the plot center toward the top of the page), and the magnitude of the speed difference determines the distance from the center. The result from experiment C is shown in Fig. 9. The next section discusses filtering the model results to remove small-scale unconstrained features, and Fig. 9 (left) is the result with no filtering applied. An accurate agreement would have a high density of occurrences just above the center of the plot. An accurate direction and poor speed would result in a distribution around the line from the plot center toward the top of the page. An accurate speed and poor direction would result with a distribution near center but to the sides or below the center. The initial comparison indicates a concentration above the plot center. Thus, there is some skill in direction with a broad distribution of errors, and mean speed difference on the order of 0.15 m/s with a relatively broad distribution as well.

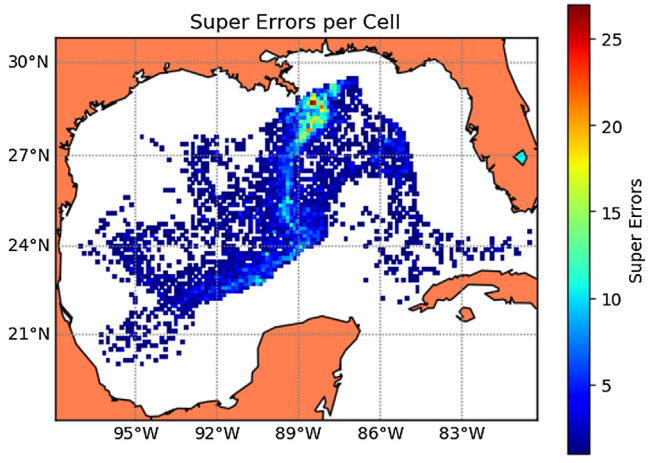

Fig. 8. The total number of super-errors in 1/8° bins over the LASER period shows the data distribution. Many of the drifters deployed in the north moved to the south and were entrained in eddies to the east and west. The analysis uses only data in water deeper than 500 m.

4. Constrained results

We determine the constrained scales by filtering features out of the model results and evaluating errors relative to LASER observations. The filtering progresses from smaller scales to larger. First, considering the PSD (Fig. 6), assume there is a wavelength λ_C that separates constrained scales at longer wavelengths from unconstrained scales at shorter wavelengths. Separate the true velocity field u into components based on this wavelength so that $u = u_C + u_U$, where u_C is the velocity field at wavelengths greater than λ_C, and u_U is the velocity field at wavelengths less than λ_C. Similarly, separate the model field into components $u' = u'_C + u'_U$, where primes indicate the model estimate of the fields. Assume that the constrained and unconstrained components are not cross-correlated in the true world or within the model. Then the model error variance is

$$Var(u - u') = \left\langle (u_C - u'_C)^2 + (u_U - u'_U)^2 \right\rangle \quad (4)$$

where $\langle\,\rangle$ indicates an expected value. Define the error of the constrained portion of the model field to be $\varepsilon_C^2 = Var(u_C - u'_C)$. If the model is realistic, then the model variance within the constrained band is equal to the true variance in the constrained band, so that $Var(u_C) = Var(u'_C)$. By definition of the constrained wavelength, the model has skill at wavelengths greater than λ_C, and therefore the error variance ε_C^2 is less than either $Var(u_C)$ or $Var(u'_C)$. Again, if the model is realistic then in the unconstrained band $Var(u_U) = Var(u'_U)$. If the model and true ocean are uncorrelated in the unconstrained band, then the model error variance in (4) is

$$Var(u - u') = \varepsilon_C^2 + 2Var(u_U) \quad (5)$$

Suppose we filter the unconstrained variability from the model. Then the error variance is

$$Var(u - (u' - u'_U)) = \varepsilon_C^2 + Var(u_U) \quad (6)$$

Please cite this article as: G. A. Jacobs, J. M. D'Addezio, B. Bartels et al., Constrained scales in ocean forecasting, Advances in Space Research, https://doi.org/10.1016/j.asr.2019.09.018

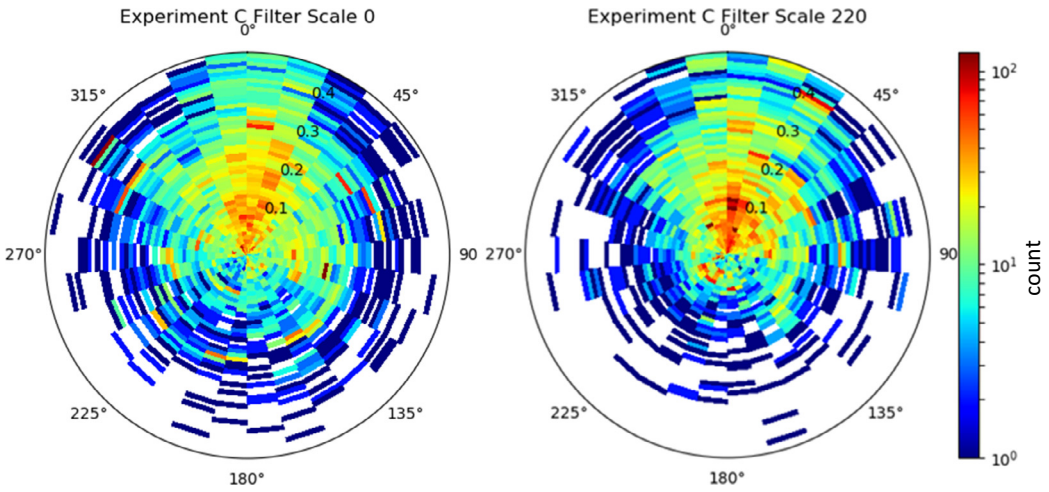

Fig. 9. The polar histogram of vector errors using experiment C relative to drifters with no filtering (left) and with 220 km ¼ power filtering (right) indicate filtering effects in improving the skill. Filtering moves the distribution toward 0 direction error (the line from the plot center toward the top of the page) and toward smaller speed differences (closer to the center). The outer edge of the histogram is a difference of 0.45 m/s.

Thus, filtering the unconstrained velocity from the model field produces a lower error variance in (6) than not filtering in (5). Suppose we over-filter the model to the point where we remove all the model variance. In this case, the error variance becomes

$$Var(u-0) = Var(u_C) + Var(u_U) \tag{7}$$

Filtering all variability produces an error variance greater than removing only the unconstrained in (6) because $\varepsilon_C^2 < Var(u_C)$. Considering the error variance from no filtering, to filtering just the unconstrained variability, to filtering all variability, filtering just the unconstrained variability produces a local minimum in the error variance as a function of filtering scale. We exploit this to determine the constrained scales by progressively filtering the model experiment velocity fields to find the minimum error variance relative to the LASER observations.

The domain of interest is irregularly shaped and finite. It is not possible to construct a filter that precisely removes variability smaller than a specified wavelength. Therefore, we use a Gaussian filter and express the results in terms of the ¼ power point of the filter (Fig. 3). The filter applied at one location uses all model data within 3 e-folding scales of the Gaussian. In areas influenced by land, the Gaussian is a weighted average of all non-land values. The filter acts on the velocity components (u and v) separately. The Gaussian function with a specified e-folding scale of l is $\exp(-x^2/l^2)$, and the ¼ power point wavelength is $L_{1/4} = \pi l/\sqrt{-\ln(1/2)} \approx 3.77l$ (Fig. 3).

For each of the five experiments, we apply a filter with ¼ power scale from 20 km to 300 km in 20 km increments. One example of the filtering of experiment C (Fig. 10) indicates the features that appear in the vorticity field computed from the filtered velocities as the filter scale is increased. The filtered surface currents determine the vorticity normalized by the Coriolis parameter, which is a Rossby number. In a geostrophic flow, the vorticity is proportional to the Laplacian of the SSH. Therefore, vorticity serves as an indicator for SSH. Using the filtered velocity fields for each experiment, the process described in the prior section provides RMS trajectory errors for each filter scale. Thus, each experiment provides one curve as a function of the filter ¼ power scale.

The results of the progressive filtering of each experiment are in Fig. 11. The experiment with the lowest RMS error for any filtering scale is experiment C, and the lowest RMS error is reached at the 220 km ¼ power scale. This corresponds to a 53 km e-folding scale of the Gaussian filter. There is consistency in the results with RMS errors increasing the more the decorrelation scale deviates from experiment C. That is, experiment A errors are larger than experiment B, which are larger than experiment C. In addition, experiment E errors are larger than experiment D errors, which are larger than experiment C.

The local minima at 220 km ¼ power scale is relatively broad for two reasons. The discussion at the beginning of this section considered a wavelength λ_C that separated constrained from unconstrained. As shown in (D'Addezio et al., 2019), errors across the wavenumber spectrum are small at the largest scales and gradually increase to the constrained wavelength and gradually rise at smaller wavelengths. There is not a sharp increase in error at the constrained wavelength. Considering a single event at one time, scales slightly larger than λ_C can be in error and scales slightly smaller can be correct. The definition of the constrained scales is based on a statistical average over time. The feature in Fig. 2 is an example. The observed cyclone is on the order of 200 km across, and on March 20, 2016 the feature is out of place from the observed. After the satellite observations of the feature correct the model, the feature is more correctly placed. Prior work has also shown that the drifters themselves are very effective in improving the solution at smaller scales (Carrier et al., 2016), and thus

Please cite this article as: G. A. Jacobs, J. M. D'Addezio, B. Bartels et al., Constrained scales in ocean forecasting, Advances in Space Research, https://doi.org/10.1016/j.asr.2019.09.018

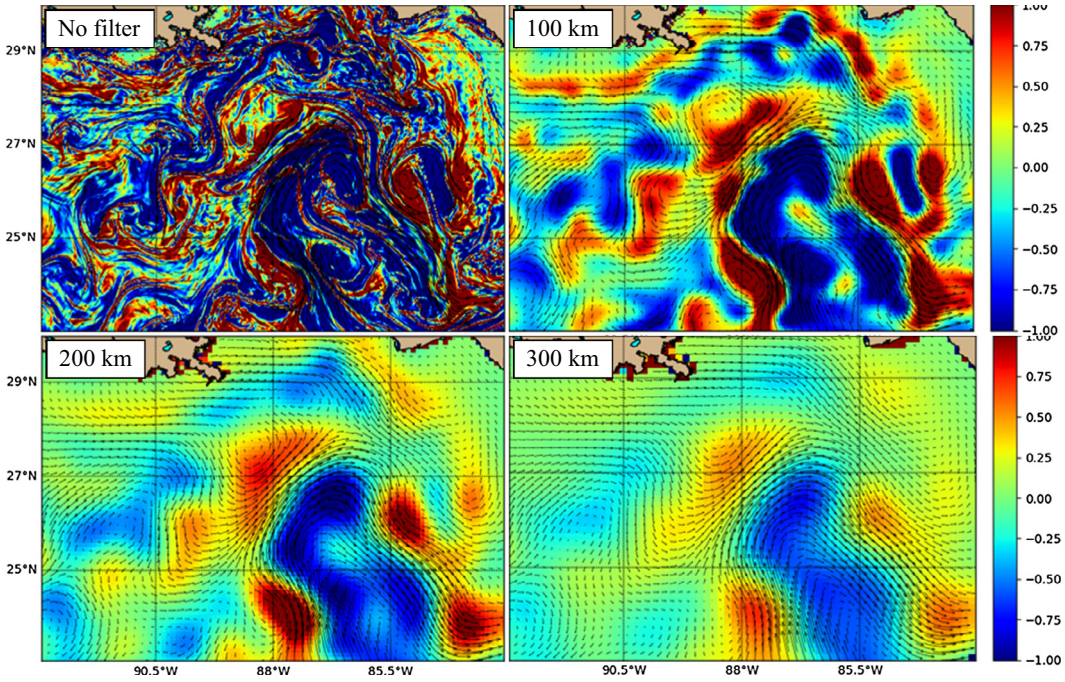

Fig. 10. The velocity field of experiment C on March 15, 2016 is shown (black vectors indicate 24 h trajectories given time-fixed model currents) after a range of no filtering to 300 km ¼ power scale filters are applied. The colored background is vorticity normalized by the Coriolis parameter (i.e. a Rossby number) based on filtered velocities.

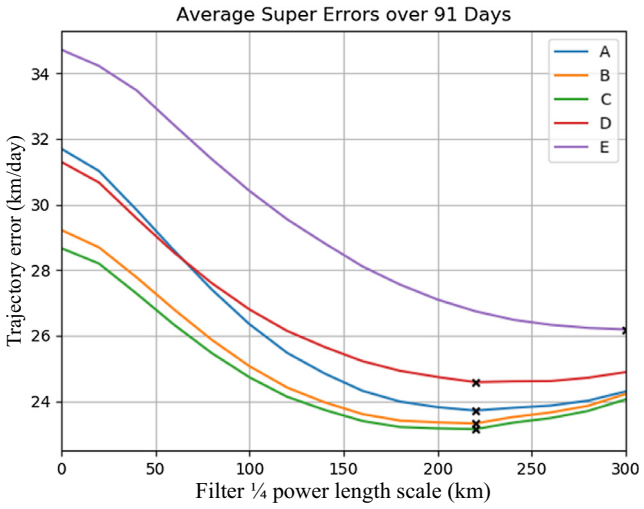

Fig. 11. RMS trajectory errors for each of the five experiments as a function of the Gaussian filter ¼ power scale. Experiment C provides the lowest errors, and most experiments (A through D) consistently have error minima at the 220 km ¼ power point of the Gaussian filter.

the results are dependent on the observing system. The second contributing factor for the broad minimum is the filtering used. Because of the irregularly shaped domain, we used a Gaussian filter that has a broad tail without a sharp spectral cutoff. When specifying an e-folding scale, the filtered fields of the model have residual effects from features at smaller scales, ultimately limiting the precision of our result.

The ¼ power scale of the minima RMS errors are consistent across experiment A through D (220 km). Experiment E has much larger errors than the other experiments, and the error minimum is at the largest scales used in filtering (300 km). Thus, experiment E is constraining only the largest features. The removal of unconstrained variability through filtering improves trajectory errors significantly for experiment C with errors reducing by 20% from just below 29 km/day with no filtering to 23 km/day at the lowest error scale. The effects of the filtering are evident in the polar error histogram plots (Fig. 9). The error histogram using filtered surface currents (right in Fig. 9) shows a greater concentration with smaller directional errors (closer to the line from the plot center toward the top of the page) and smaller magnitude of speed errors (closer to the plot center) when compared to the unfiltered error histogram (left in Fig. 9). Note that the error levels are large relative to prior publications that consider errors relative to ARGO drifters because of the surface intensification of currents and the effects of wind events during the winter period of the deployment. The Gulf of Mexico is also an area of higher mesoscale variability, due to the Atlantic Sverdrup transport passing through, and this adds to higher than average error levels as well.

5. Summary and conclusions

Our primary objective has been to determine the scales at which present observing systems constrain ocean forecasts. Five ocean data assimilation experiments were conducted with differing horizontal decorrelation scales, and the results were evaluated against velocity observations from 1000 surface drifters. All satellite and in situ observa-

Please cite this article as: G. A. Jacobs, J. M. D'Addezio, B. Bartels et al., Constrained scales in ocean forecasting, Advances in Space Research, https://doi.org/10.1016/j.asr.2019.09.018

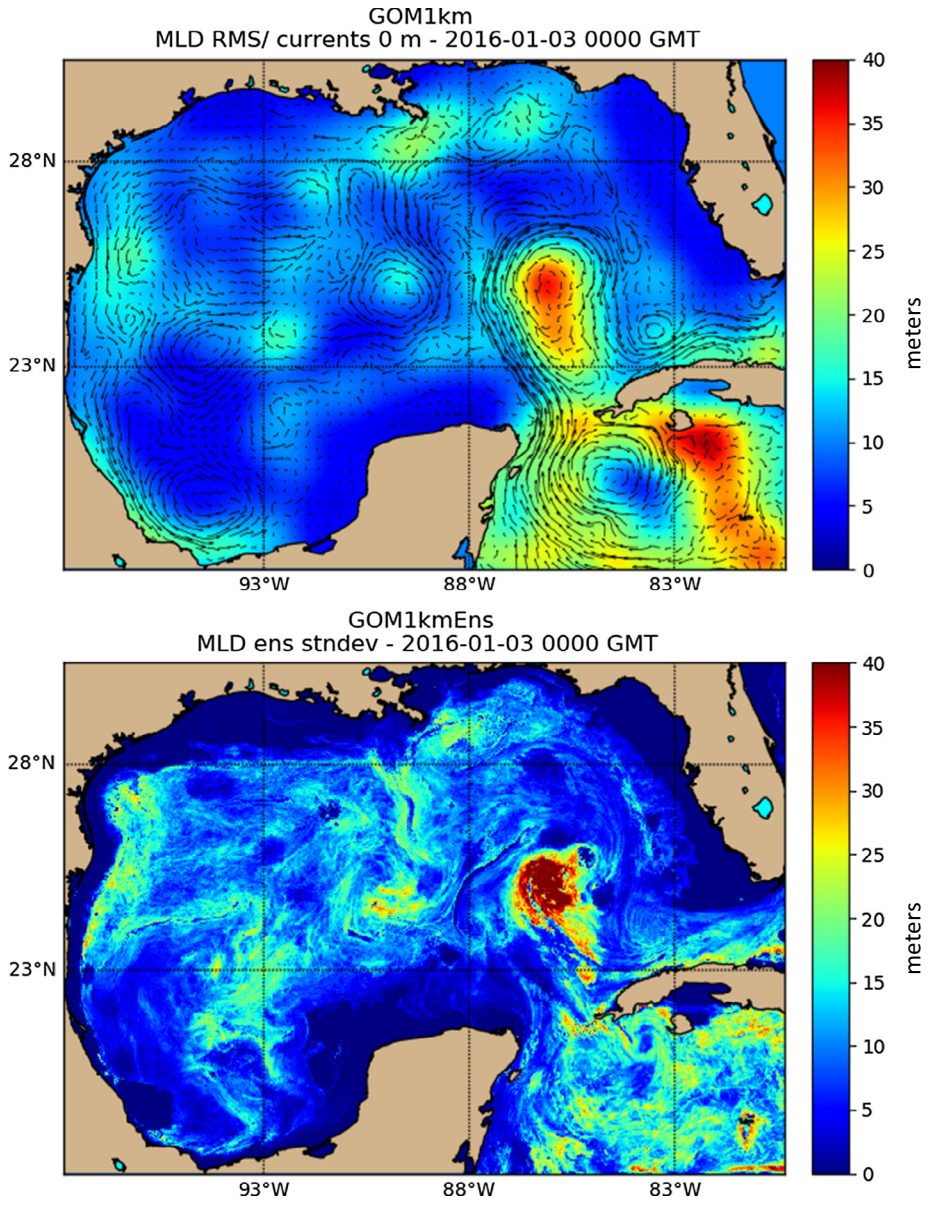

Fig. 12. A comparison of (top) unconstrained mixed layer depth spatial variability in the 1 km experiment C used here to (bottom) the RMS variability across a 3 km resolution ensemble set. The small-scale variability (top) has significant amplitude relative to the ensemble estimate of RMS (bottom) indicating that the small-scale structure is a significant contributor to forecast errors.

tions during October 2015–April 2016 were used in the experiments, and the surface drifters during January–April 2016 were withheld for evaluation. The constrained scales are determined by filtering unconstrained variability from numerical model results. A SOAR decorrelation scale of 36 km used in the data assimilation along with a Gaussian filter of ¼ power scale of 220 km, which is an e-folding scale of 58 km, results in the lowest errors relative to LASER drifter observations. While the determined scale is a local minimum and is consistent across the experiments, the minimum is relatively broad. The implication is that errors do not change rapidly as a function of length scale.

The scales our unique experimentation provides are similar to those determined by fraternal twin OSSE experiments (D'Addezio et al., 2019). This indicates that the primary source of error in ocean forecast systems is the data density and its ability to constrain features. The errors induced by uncertainties in numerical model representation certainly exist and are important. However, the dynamical errors absent within the fraternal twin OSSEs did not prevent similar results with the approach used here. Of course, the only evaluation in this study is surface currents. Consideration of other variables may lead to different conclusions.

The simple filtering to remove unconstrained variability demonstrates a 20% reduction in RMS trajectory error. Operational applications could benefit from such an approach. As we look to SWOT observations or other targeted observing systems providing dense patchy data, a

Please cite this article as: G. A. Jacobs, J. M. D'Addezio, B. Bartels et al., Constrained scales in ocean forecasting, Advances in Space Research, https://doi.org/10.1016/j.asr.2019.09.018

multiscale analysis would appropriately use the decorrelation scale determined here (36 km) in the first of a sequential analysis to correct the larger scale features. The SWOT observations could then correct smaller scale structure in the forecast system.

As is typically the case, these results are region specific. The Gulf of Mexico resides in the subtropics. Scales are slightly larger to the south and smaller to the north. Additionally, the spacing between satellite tracks decreases with latitude. Therefore, there may be compensating effects that users should heed.

Finally, we would be negligent if we did not address a potential, and ultimately incorrect, interpretation of our results with respect to model resolution. If the data provided to a cycling assimilation/forecast system can only constrain a limited range of scales, why should operational centers run models with any higher resolution? The small features in a high-resolution forecast are important for many operations, and the small-scale features are significant contributors to forecast errors. For operational application, we need to know the effects of the small-scale errors. The predictability in the unconstrained variability is statistical since the large-scale features modulate the small-scale. The deeper mixed layer in anticyclonic versus cyclonic mesoscale eddies modulate submesoscale eddies. The predictable information for the small-scale is the spatial density distribution given the modulation by the constrained large-scale.

An example at one time (Fig. 12) compares the square root of spatial variance at scales smaller than the constrained (58 km e-folding scale) in the 1 km experiment C to the standard deviation across a 32 member ensemble at 3 km resolution (Wei et al., 2014). The general areas of high forecast error estimated from the ensemble and areas of high unconstrained variability roughly coincide, and the unconstrained variability in the 1 km result has amplitudes that are significant relative to the ensemble estimates. Ensemble systems usually are restricted to much lower resolution due to computational requirements and therefore cannot represent the full spectrum of energy. Forecast errors in the constrained features are represented in ensembles but not the high resolution run. High resolution models contain the unconstrained variability but do not provide error estimates of the constrained scales. Ensembles and unconstrained energy together give a more complete picture of forecast errors. In addition to contributing to the forecast errors, the nonlinear interactions of large- and small-scale dictate the forecast evolution of the constrained flow. Therefore, important operational capabilities are possible only if the model resolution is sufficient to represent both the large- and small-scale features.

Acknowledgments

This research is funded by the NRL work unit Submesoscale Prediction of Eddies from Altimeter Retrieval (SPEAR) and a grant from BP/The Gulf of Mexico Research Initiative to the Consortium for Advanced Research on the Transport of Hydrocarbon in the Environment (CARTHE). This paper is contribution NRL/JA-7320-19-4383 and has been approved for public release. Model data during the LASER experiment may be obtained through the Gulf of Mexico Research Initiative archival site at https://data.gulfresearchinitiative.org under DOI number: https://doi.org/10.7266/N7HQ3WZR. The LASER drifter data is available through the DOI numbers https://doi.org/10.7266/N7W0940J and https://doi.org/10.7266/N7QN656H.

References

Atlas, R., Bucci, L., Annane, B., Hoffman, R., Murillo, S., 2015. Observing system simulation experiments to assess the potential impact of new observing systems on hurricane forecasting. Mar. Technol. Soc. J. 49 (6), 140–148.

Bell, M.J., Schiller, A., Le Traon, P.-Y., Smith, N., Dombrowsky, E., Wilmer-Becker, K., 2015. An introduction to GODAE OceanView. J. Oper. Oceanogr. 8 (sup1), 10. https://doi.org/10.1080/1755876X.2015.1022041.

Carrier, M.J., Ngodock, H.E., Muscarella, P., Smith, S., 2016. Impact of assimilating surface velocity observations on the model sea surface height using the NCOM-4DVAR. Mon. Weather Rev. 144 (3), 1051–1068.

Chelton, D.B., Deszoeke, R.A., Schlax, M.G., El Naggar, K., Siwertz, N., 1998. Geographical variability of the first baroclinic Rossby radius of deformation. J. Phys. Oceanogr. 28 (3), 433–460.

D'Addezio, J.M., Smith, S., Jacobs, G.A., Helber, R.W., Rowley, C., Souopgui, I., Carrier, M.J., 2019. Quantifying wavelengths constrained by simulated SWOT observations in a submesoscale resolving ocean analysis/forecasting system. Ocean Model. 135, 40–55.

D'Asaro, E.A., Shcherbina, A.Y., Klymak, J.M., Molemaker, J., Novelli, G., Guigand, C.M., Haza, A.C., Haus, B.K., Ryan, E.H., Jacobs, G. A., 2018. Ocean convergence and the dispersion of flotsam. Proc. Natl. Acad. Sci. 115 (6), 1162–1167.

Egbert, G.D., Erofeeva, S.Y., 2002. Efficient inverse Modeling of barotropic ocean tides. J. Atmos. Ocean. Tech. 19 (2), 183–204.

Fox, D.N., Teague, W.J., Barron, C.N., Carnes, M.R., Lee, C.M., 2002. The modular ocean data assimilation system (MODAS). J. Atmos. Ocean. Tech. 19 (2), 240–252.

Gaultier, L., Ubelmann, C., Fu, L.-L., 2016. The challenge of using future SWOT data for oceanic field reconstruction. J. Atmos. Ocean. Tech. 33 (1), 119–126.

Haza, A.C., D'Asaro, E., Chang, H., Chen, S., Curcic, M., Guigand, C., Huntley, H., Jacobs, G., Novelli, G., Özgökmen, T., 2018. Drogue-loss detection for surface drifters during the Lagrangian submesoscale experiment (LASER). J. Atmos. Ocean. Tech. 35 (4), 705–725.

Hodur, R.M., 1997. The Naval Research Laboratory's coupled ocean/atmosphere mesoscale prediction system (COAMPS). Mon. Weather Rev. 125 (7), 1414–1430.

Jacobs, G., Barron, C., Rhodes, R., 2001. Mesoscale characteristics. J. Geophys. Res. Oceans (1978–2012) 106 (C9), 19581–19595.

Jacobs, G.A., Bartels, B.P., Bogucki, D.J., Beron-Vera, F.J., Chen, S.S., Coelho, E.F., Curcic, M., Griffa, A., Gough, M., Haus, B.K., 2014. Data assimilation considerations for improved ocean predictability during the Gulf of Mexico Grand Lagrangian Deployment (GLAD). Ocean Model. 83, 98–117.

Jacobs, G.A., Huntley, H.S., Kirwan, A., Lipphardt, B.L., Campbell, T., Smith, T., Edwards, K., Bartels, B., 2016. Ocean processes underlying surface clustering. J. Geophys. Res. Oceans 121 (1), 180–197.

Le Traon, P.-Y., Dibarboure, G., Jacobs, G., Martin, M., Rémy, E., Schiller, A., 2017. Use of satellite altimetry for operational oceanog-

raphy. In: Satellite Altimetry Over Oceans and Land Surfaces. CRC Press, Boca Raton, pp. 581–608.

Li, Z., McWilliams, J.C., Ide, K., Farrara, J.D., 2015. A multiscale variational data assimilation scheme: formulation and illustration. Mon. Weather Rev. 143 (9), 3804–3822.

Martin, P.J., Barron, C.N., Smedstad, L.F., Campbell, T.J., Wallcraft, A. J., Rhodes, R.C., Rowley, C., Townsend, T.L., Carroll, S.N., 2009. User's manual for the Navy Coastal Ocean Model (NCOM) version 4.0Rep. Naval Research Lab Stennis Space Center MS Ocean Dynamics and Prediction Branch.

Metzger, E., Hurlburt, H., Wallcraft, A., Shriver, J., Townsend, T., Smedstad, O., Thoppil, P., Franklin, D., Peggion, G., 2010. Validation test report for the global ocean forecast system V3Rep., 0–1/12 HYCOM/NCODA: Phase II, NRL Memo. Rep. NRL/MR/7320–10-9236. Nav. Res. Lab., Stennis Space Center, Miss. http://www7320.nrlssc.navy.mil/pubs/2010/metzger1-2010.pdf.

Novelli, G., Guigand, C.M., Cousin, C., Ryan, E.H., Laxague, N.J., Dai, H., Haus, B.K., Özgökmen, T.M., 2017. A biodegradable surface drifter for ocean sampling on a massive scale. J. Atmos. Ocean. Tech. 34 (11), 2509–2532.

Özgökmen, T.M., Boufadel, M., Carlson, D.F., Cousin, C., Guigand, C., Haus, B.K., Horstmann, J., Lund, B., Molemaker, J., Novelli, G., 2018. Technological advances for ocean surface measurements by the Consortium for Advanced Research on Transport of Hydrocarbons in the Environment (CARTHE). Mar. Technol. Soc. J. 52 (6), 71–76.

Özgökmen, T.M., Chassignet, E.P., Dawson, C.N., Dukhovskoy, D., Jacobs, G., Ledwell, J., Garcia-Pineda, O., MacDonald, I.R., Morey, S.L., Olascoaga, M.J., 2016. Over what area did the oil and gas spread during the 2010 Deepwater Horizon oil spill? Oceanography 29 (3), 96–107.

Richman, J.G., Arbic, B.K., Shriver, J.F., Metzger, E.J., Wallcraft, A.J., 2012. Inferring dynamics from the wavenumber spectra of an eddying global ocean model with embedded tides. J. Geophys. Res. Oceans 117 (C12), C12012.

Rowley, C., Mask, A., 2014. Regional and coastal prediction with the relocatable ocean nowcast/forecast system. Oceanography 27 (3), 44–55.

Smith, S., Cummings, J., Rowley, C., Chu, P., Shriver, J., Helber, R., Spence, P., Carroll, S., Smedstad, O., Lunde, B., 2011. Validation Test Report for the Navy Coupled Ocean Data Assimilation 3D Variational Analysis (NCODA-VAR) System, Version 3.43Rep. NRL Report NRL/MR/7320-11-9363, Naval Research Laboratory, Stennis Space Center, MS.

Thoppil, P.G., Richman, J.G., Hogan, P.J., 2011. Energetics of a global ocean circulation model compared to observations. Geophys. Res. Lett. 38 (15), L15607.

Wei, M.Z., Rowley, C., Martin, P., Barron, C.N., Jacobs, G., 2014. The US Navy's RELO ensemble prediction system and its performance in the Gulf of Mexico. Q. J. Roy. Meteor. Soc. 140 (681), 1129–1149.

Please cite this article as: G. A. Jacobs, J. M. D'Addezio, B. Bartels et al., Constrained scales in ocean forecasting, Advances in Space Research, https://doi.org/10.1016/j.asr.2019.09.018

Please cite this article as: G. A. Jacobs, J. M. D'Addezio, B. Bartels et al., Constrained scales in ocean forecasting, Advances in Space Research, https://doi.org/10.1016/j.asr.2019.09.018